International Journal of Nanomedicine

Dovepress
open access to scientific and medical research

Open Access Full Text Article

ORIGINAL RESEARCH

Glutathione Depletion-Induced ROS/NO Generation for Cascade Breast Cancer Therapy and Enhanced Anti-Tumor Immune Response

Jing Wang[1,*], Yanxiang Sang[2,*], Weijian Chen[3], Liang Cheng[2], Wenxiang Du[2], Hongjie Zhang[2], Benyan Zheng[2], Lei Song[2], Yuan Hu[2], Xiaopeng Ma[1]

[1]Department of General Surgery, The First Affiliated Hospital of USTC, Division of Life Sciences and Medicine, University of Science and Technology of China, Hefei, Anhui, 230001, People's Republic of China; [2]State Key Laboratory of Fire Science, University of Science and Technology of China, Hefei, Anhui, 230006, People's Republic of China; [3]Technology Center, China Tobacco Anhui Industrial Co, Ltd, Hefei, Anhui, 230088, People's Republic of China

*These authors contributed equally to this work

Correspondence: Yuan Hu; Xiaopeng Ma, Email yuanhu@ustc.edu.cn; XiaopengMa@fsyy.ustc.edu.cn

Introduction: As an effective alternative choice to traditional mono-therapy, multifunctional nanoplatforms hold great promise for cancer therapy. Based on the strategies of Fenton-like reactions and reactive oxygen species (ROS)-mediated therapy, black phosphorus (BP) nanoplatform BP@Cu_2O@L-Arg (BCL) co-assembly of cuprous oxide (Cu_2O) and L-Arginine (L-Arg) nanoparticles was developed and evaluated for synergistic cascade breast cancer therapy.

Methods: Cu_2O particles were generated in situ on the surface of the BP nanosheets, followed by L-Arg incorporation through electrostatic interactions. In vitro ROS/nitric oxide (NO) generation and glutathione (GSH) depletion were evaluated. In vitro and in vivo anti-cancer activity were also assessed. Finally, immune response of BCL under ultrasound was investigated.

Results: Cu_2O was incorporated into BP to exhaust the overexpressed intracellular GSH in cancer cells via the Fenton reaction, thereby decreasing ROS consumption. Apart from being used as biocompatible carriers, BP nanoparticles served as sonosensitizers to produce excessive ROS under ultrasound irradiation. The enhanced ROS accumulation accelerated the oxidation of L-Arg, which further promoted NO generation for gas therapy. In vitro experiments revealed the outstanding therapeutic killing effects of BCL under ultrasound via mechanisms involving GSH deletion and excessive ROS and NO generation. In vivo studies have illustrated that the nanocomplex modified the immune response by promoting macrophage and CD8+ cell infiltration and inhibiting MDSC infiltration.

Discussion: BCL nanoparticles exhibited multifunctional characteristics for GSH depletion-induced ROS/NO generation, making a new multitherapy strategy for cascade breast cancer therapy.

Keywords: black phosphorus, combination cancer therapy, sonodynamic therapy, chemodynamic therapy, nitric oxide gas therapy

Introduction

High concentrations of toxic reactive oxygen species (ROS) have been widely applied to induce oxidative damage and apoptosis.[1,2] Based on this approach, innovative therapeutic strategies including photodynamic therapy (PDT),[2] sonodynamic therapy (SDT),[3] and chemical dynamic therapy (CDT)[4] have been developed as powerful alternatives for cancer therapy. Owing to the limitations of monotherapy, researchers have focused on synergistic therapies to achieve the effect of 1+1>2.[5] Black phosphorus (BP), a two-dimensional nanomaterial, exhibits excellent light-absorption performance, high photothermal conversion efficiency, biodegradability, and large specific surface area.[6] BP can be gradually degraded into phosphate ions under physiological conditions without biological toxicity.[7] Owing to its multiple outstanding properties, BP has shown great potential in the biomedical field for PTT, PDT, and SDT applications.[8,9] Compared with light-mediated PTT or PDT, SDT and SDT-based combination therapy have the advantages of higher tissue penetration and minimal invasiveness. Thus, SDT is considered of great significance for cancer therapy.[10–12]

Received: 9 October 2023
Accepted: 29 February 2024
Published: 7 March 2024

Numerous studies have confirmed that BP, as a sonosensitizer, can induce ROS generation in cancer therapy, concomitantly inducing stronger immunogenicity.[13–16]

Owing to the high proliferative capacity of cancer cells, the tumor microenvironment is characterized by abnormally high concentrations of glutathione (GSH) and hydrogen peroxide (H_2O_2).[17–19] High GSH levels in cancer cells have been known to readily capture ROS in the cellular environment to generate oxidized glutathione disulfide (GSSG), resulting in a compromised effect of ROS therapy.[20–24] Therefore, it is important to enhance the antioxidant GSH consumption to facilitate ROS generation and achieve the desired ROS-based therapy.

CDT is a type of Fenton or Fenton-like reaction mediated by Fe^{2+}, Cu^{+}, or Mn^{2+}, based on the acidity of the tumor microenvironment and high concentrations of H_2O_2.[25–27] Moreover, the Fenton reaction is independent of the oxygen or external energy. The environment of normal cells (pH and the concentration of H_2O_2) is not suitable for the Fenton reaction, which is therefore beneficial for normal cell protection. Fe^{2+}-mediated Fenton reaction is limited by the relatively strict acidic environment and low reaction rate.[28] However, the Cu^{+}-catalyzed Fenton reaction converts H_2O_2 into OH at a high reaction rate, even in a neutral environment. The reaction efficiency can reach 160 times than that of Fe^{2+}.[29] In addition, Cu^{+}/Cu^{2+} has a lower redox potential, which facilitates Cu^{+}/Cu^{2+} cycling in the tumor environment.[30] Therefore, Cu^{2+}-mediated CDT is a promising strategy to consume high GSH content in cancer cells, thereby improving the therapeutic efficiency of ROS-based therapy.

Gas therapy has attracted widespread attention as an emerging therapeutic approach. It is known to be minimally toxic to normal organs and beneficial to metabolism. Currently, nitric oxide (NO),[31] carbon monoxide (CO),[32] and hydrogen sulfide (H_2S)[33] are the main transmitters used in gas therapy. As the first gaseous mediator recognized as a biological mediator, NO plays a prominent role in vascular regulation, wound healing, physiological and pathophysiological processes. L-arginine (L-Arg) is an excellent biocompatible source of NO, which is one of the 21 amino acids in the human body. L-Arg can be catalyzed to generate NO by ultrasound, ROS, or NO synthase.[34] Furthermore, recent studies have illustrated that NO can modulate the tumor immunosuppressive microenvironment by regulating immune cell infiltration, suggesting the immunomodulatory activity of NO in the tumor immune microenvironment.[35,36]

Based on the above strategies, we designed a BP nanosheet-based composite BP@Cu_2O@L-Arg (BCL) that integrates sonodynamic/chemodynamic/gas/immune therapy for cascade breast cancer treatment. The lamellar structure of 2D BP provided a platform for further modifications and drug loading. First, Cu_2O particles were generated in situ on the surface of the BP nanosheets to harvest BP-Cu_2O (BC), followed by incorporation of L-Arg into BC through electrostatic interactions to obtain BCL. In this platform, BP nanosheets not only served as a platform to integrate Cu_2O and L-Arg but also acted as sonosensitizers for ROS generation. On the one hand, cuprous oxide consumed GSH by Fenton reaction, which further increased the level of ROS. The cascade amplification of ROS rapidly oxidized L-Arg and promoted NO production, further improving its inhibitory effects on cancer cells. Bioinformatics and subsequent flow cytometry analyses revealed enhanced immune-regulatory effects of BCL plus SDT therapy (Scheme 1). Therefore, breast cancer cascade therapy based on glutathione depletion-induced ROS/NO generation can be considered as an enhanced strategy for anti-tumor treatment.

Materials and Methods

Materials

Red phosphorus (98%), stannic iodide (95%), tin powder, N-methyl pyrrolidone (NMP), Cupric Acetate Monohydrate, Vitamin C, L-Arginine (L-Arg), glutathione (GSH), and 5.5'-Dithiobis-(2-nitrobenzoic acid) (DTNB) were purchased from Aladdin Reagent (Shanghai) Co. Ltd. Hydrogen Peroxide (H_2O_2), 9.10-Anthracenediyl-bis(methylene) dimalonic acid (ABDA), P-phthalic acid (PTA), Griess reagent (Beyotime nitric oxide detection kit), propidium iodide (PI), calcein acetoxymethyl ester (Calcein-AM), 2.7-dichlorofluorescin diacetate (DCFH-DA), 3-Amino, 4-aminomethyl-2′, 7′-difluorescein, diacetate (DAF-FM DA) were purchased from Beyotime Institute of Biotechnology (Shanghai, China). The 4T1 breast tumor cells were commercially purchased from Cellverse Bioscience Technology Co., Ltd.

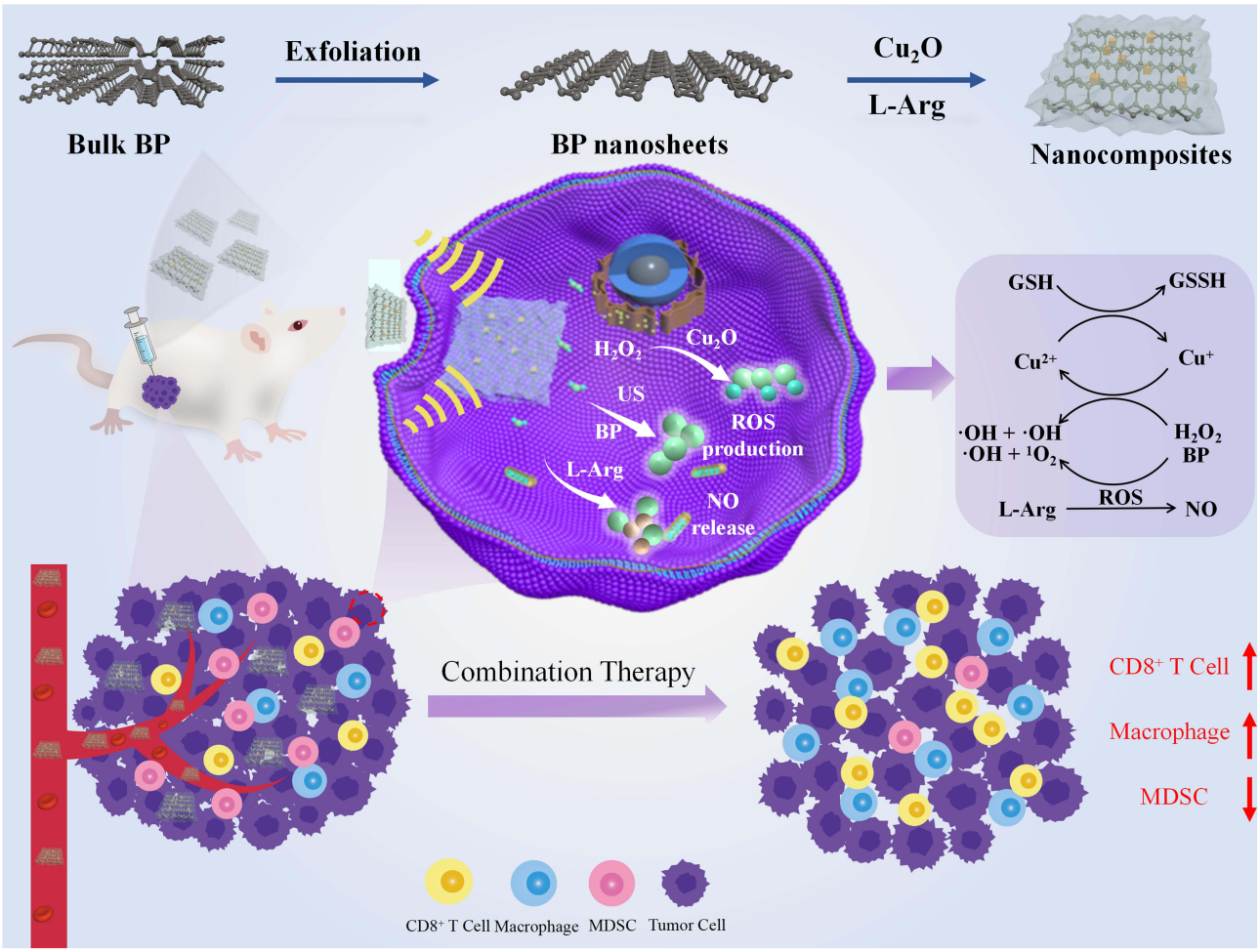

Scheme 1 Schematic illustration of BCL composites synthesis procedure and the anti-cancer mechanisms including BP-based ROS generation, GSH deletion, NO production, enhanced anti-cancer immune response.

Characterization

The morphologies of BP and BCL were assessed by transmission electron microscopy (TEM) (JEM-2100 F, Japan Electron Optics Laboratory Co., Ltd., Japan). The morphologies of BCL were observed by a PHILIPS XL30E scanning electron microscope (SEM). Fourier transform infrared (FT-IR) spectra (4000–500 cm single bond1) were recorded using a Nicolet 6700 spectrometer (Nicolet Instrument Co., USA). X-ray diffraction (XRD) patterns were obtained using an X-ray diffractometer (Rigaku Co., Japan) with Cu Kα radiation (λ = 0.15418 nm) at a scanning rate of 4°·min single bond1. Raman spectra were recorded using a laser micro-Raman spectrometer (Jobin Yvon Co., Ltd., France). The zeta potentials of the samples were determined by the Dynamic Light Scattering Instrument (NanoBrook 90 Plus PALS, Brookhaven). Fluorescence spectra were recorded using a fluorometer (F-7100 FL Spectrophotometer, Hitachi).

The Bulk BP and BP Nanosheets Synthesis

Bulk BP was synthesized as follows: red phosphorus was mixed with Sn/SnI_4 and sealed in vacuum quartz tubes, which were placed in a tubular furnace at a high temperature for programmed heating. The temperature was raised to 650°C in 4 h. Afterwards, the temperature was reduced to 500°C and maintained for 2 h. BP crystals were naturally cooled down to room temperature for subsequent use. The bulk BP was finely ground and washed with toluene and acetone. One hundred milligram BP was dispersed in an anhydrous NMP (100 mL NMP for ultrasonication for 12 h in an ice bath). The suspension was then centrifuged at 5000 rpm for 10 min. The supernatant was collected and centrifuged again at 11,000

rpm to obtain BP nanosheets. The BP nanosheets were washed with deionized water and anhydrous ethanol and stored in an inert gas atmosphere.

Synthesis of BCL

About 0.25 mmol of copper acetate monohydrate was dispersed in 50 mL of deionized water, and the copper acetate solution was added to 100 mg of BP dispersion. A sodium hydroxide solution was added dropwise, and the mixture was stirred for 10 min. Subsequently, 200 mg of ascorbic acid was added, and the reaction was continued for half an hour. After washing to obtain the black phosphorus complex, BC was loaded with cuprous oxide. L-Arg (100 mg) was added, and the mixture was stirred for 4 h to collect BCL.

The Accumulated Releases of Cu

The release of Cu ions was measured using dialysis. BCL was dispersed in deionized water at different pH values. The solution was collected at a specific time, and the copper ion content was determined using ICP-OES.

BP Composites Sonodynamic Properties

ABDA was added to BCL in the dark and exposed to US irradiation (1.0 MHz, 50% duty cycle, 1.5 $W \cdot cm^{-2}$) for 3 min. The OH generation was assessed using PTA. The fluorescence spectra were recorded.

Fenton Reaction

TMB was used to record the formation of Cu^{+}-catalyzed Fenton-like reactions associated with ·OH. Briefly, BCL ([Cu] = 0.4×10^{-3} M) was dispersed in a phosphate buffer (pH 5.5). The suspension was shaken for 1 h at 37°C. H_2O_2 and TMB were added after centrifugation. The generation of ·OH was recorded using an ultraviolet (UV) spectrophotometer. The control groups were TMB + BC (pH 5.5), TMB + BC (pH 7.4), TMB + H_2O_2 (pH 5.5), TMB+ H_2O_2 (pH 7.4), TMB + BC + H_2O_2 (pH 5.5), and TMB + BC + H_2O_2 (pH 7.4).

GSH Consumption

BC was dispersed in 6 mL GSH solution (1.5 mM, pH = 7) at 37°C. The supernatant (0.5 mL) was collected from the solution after centrifugation for 0, 3, 6, 9, and 12 min. Subsequently, 2.5 mL PBS, and 50 μL 5.5'-dithiobis-(2-nitrobenzoic acid) (10 mM; DTNB was used as the indicator of GSH) was added to the supernatant. UV–vis spectra were recorded.

Assessment of NO Generation

A standard curve was plotted for NO concentration quantification. BCL was dispersed in PBS and irradiated with US (1.0 MHz, 50% duty cycle, 1.5 W/cm^2) for 3 minutes. Griess agent was added, and the absorbance at 560 nm was detected using a microplate reader. Control groups including PBS, BCL, and L-Arg with or without US irradiation were used for comparison.

Cellular Uptake of Nanocomposites

The 4T1 breast tumor cells were seeded onto coverslips in a 6-well plate. The cells were incubated overnight, and Rhodamine 6G dye-loaded BP nanosheets (NSs) were added for 0, 1, 2, and 4 h. The cells were then washed with PBS, and the nuclei were stained with DAPI. Fluorescence was recorded using a confocal laser-scanning microscopy (Zeiss, LSM980).

Cell Cytotoxicity Assay

The 4T1 cells were seeded into 96-well plates. When stayed tightly, the cells were treated with an increased concentration of BCL (0, 10, 20.40 60 80.10 μg/mL) for 24 h. For sonodynamic therapy assessment, 40μg/mL L-Arg, BC, BCL were added to 96-well plates containing 4T1 cells and co-cultured for 2 h. Cells were then subjected to ultrasound irradiation for 10 min (1.0 MHz, 50% duty cycle, 1.5 W/cm^2) in a specially designed tank as reported in previous study to dissipate heat caused affection.[37] After continuous culture for 24 h, cell viability was evaluated using CCK8 (C0042, Beyotime) according to the manufacturer's instructions.

Detection of Intracellular ROS, GSH, and NO

The cells were seeded in 6-well plates and incubated overnight. For ROS detection, 4T1 cells were co-cultured with 40μg/mL of BP, BC, BCL, BC+US, or BCL+US. After incubation for 2 h, cells were subjected to US irradiation (1.0 MHz, 50% duty cycle, 1.5 W/cm^2) for 10 min in the forementioned tank. The cells were stained with DCFH-DA (S0033S, Beyotime) according to the manufacturer's instructions. NO generation in 4T1 cells treated with BP, BC, BCL, BC+US, and BCL+US were determined using a NO kit (S0021S, Beyotime). Images were captured by fluorescence microcopy (NIB610-FL). The ROS and NO fluorescence intensity were also measured via a flow cytometer. For GSH detection, the cells were treated with BP, BC, BCL, BC+US, and BCL+US and incubated for 24 h. GSH was detected using a GSH and GSSG Assay Kit (S0053, Beyotime).

In vivo Anti-Tumor Effect

The animal models were approved by the Regulations for the Administration of Affairs Concerning Experimental Animals (Hefei, revised in June 2013). Briefly, 2×10^6 4T1 cells were mixed with Matrigel (1:1) and injected into the right flank of mice. 4T1-bearing mice were locally injected with nanomaterials containing PBS, L-Arg, BC, and BCL. Tumor volume (V) was calculated every 2 days using the following equation: $V = (L \times W^2)/2$ (L and W refer to the longest and shortest dimensions of the tumor). When the tumor volume reached approximately 100 mm^3, mice were randomly divided into six groups. Nanomaterials (PBS, L-Arg, BC, BC + US, BCL, and BCL+US) were locally injected at 5 mg/kg on days 0 and 5. Ultrasonication was performed for 3 min at a density of 1.5 W/cm^2 6 h after injection. The mice were sacrificed 10 days after administration. Tumors and major organs were collected for hematoxylin–eosin staining (H&E) staining or dihydroethidium (DHE) staining (Aike Biological Technology Co., Ltd.).

Next-Generation RNA Sequencing (RNA-Seq) and Bioinformatic Analysis

Total RNA was prepared using the TRIzol reagent. Paired-end libraries, library construction, and sequencing were conducted by Sinotech Genomics Co., Ltd. (Shanghai, China). Gene expression analysis was performed using the edgeR package. Differentially expressed genes were identified with a cutoff of $|\log2(\text{FoldChange})| > 1.0$ and $q < 0.05$. Kyoto Encyclopedia of Genes and Genomes (KEGG) enrichment pathway analyses were performed using KEGG functions in the R package. Gene set enrichment analysis (GSEA) was performed according to guidelines (http://www.broadinstitute.org/gsea/index.jsp). The gene sets were obtained from the Molecular Signature Database (MSigDB).

Isolation of Immune Cells of Mouse Breast Tumor Tissue

Fresh tumor samples were collected and cut into pieces. The pieces were digested with the Type IV collagenase (Sigma-Aldrich, C5138) at a concentration of 1 mg/mL in RPMI 1640, using a vibrating microtome at 37°C, 180 rpm for 120 min. The mixture was filtered through 200 μm pore-size cell strainers and centrifuged at 1500 rpm at 4°C for 5 min. The cell precipitate was resuspended in 6–8 mL of 40% Percoll solution (17,089,109 GE Healthcare). The suspension was then centrifuged at 2000 rpm for 20 min at room temperature. The supernatants were collected and centrifuged at 2000 rpm for 5 min in pre-cooled PBS. The cell pellets were resuspended in 10 mL PBS to obtain cell pellets, which were resuspended with 1.0 mL ice-cold PBS again. A minimum of 1.0×10^6 cells were stained for flow cytometry.

Flow Cytometry Analysis of Immune Response

The tumor cells were centrifuged at 6000 rpm for 2 min at 4°C and resuspended in 30 μL block buffer (2‰ BSA in FBS buffer) for 15 min in the dark. Twenty milliliters of the cell mixture were collected as the unstained control group. The remaining samples were analyzed with antibody cocktails for staining to detect CD45, CD11b, F4/80, CD206, or combinations of CD45, CD3, CD8, and CD19 (BioLegend, San Diego, CA). Typically, 30μL of the antibody cocktail solution was added to each sample, and the mixture was incubated on ice for 20 min in the dark. Tubes were shaken, and cells were centrifuged at 6000 rpm for 2 min at 4°C. The cells were washed with 1.0 mL of FBS buffer. Cell pellets were resuspended in 400 μL FBS buffer and analyzed using BD Fortessa. FACS data were analyzed using the CytExpert software (Beckman Coulter, version 2.4).

Experiment Ethics

Animal experiments were conducted according to the Guidelines for the Care and Use of Laboratory Animals of the University of Science and Technology of China. This study was approved by the Ethics Committee of the University of Science and Technology of China (USTCACUC202301002).

Statistical Analysis

GraphPad Prism was used for statistical analysis. The results were expressed as means ± standard deviation (SD). Differences were analyzed using unpaired Student's t-tests and One-way ANOVA. $p < 0.05$ was considered statistically significant. *p < 0.05, **p < 0.01, ***p < 0.001. ****p < 0.0001.

Results and Discussion

Construction and Characterization of BCL

The BP nanosheets were harvested through ultrasound-assisted liquid-phase exfoliation. The BP nanosheets exhibited an obvious two-dimensional sheet structure with a nanometer size (453.2 nm). Moreover, an obvious layer interface can be observed, which was ascribed to the inherent characteristics of 2D BP in Figure 1A. As shown in Figure 1B, after Cu_2O and L-Arg were loaded onto the surface of BP, cubic cuprous oxide (approximately 49.2 nm) was observed on the surface, with a narrow cuprous oxide size distribution. In addition, the surface modification had no significant effect on the morphology of the BP nanosheets. Figure 1C shows the lattice fringes of Cu_2O obtained using high-resolution transmission electron microscopy. The lattice spacing measured 0.25 nm,[38] which was attributed to the (111) plane of Cu_2O. The prominent vibrations at 360.2 cm^{-1}, 438.1 cm^{-1}, and 464.4 cm^{-1} were attributed to the A_g^1, B_{2g}, and A_g^2 modes of BP nanosheets, respectively, in Figure 1D. As shown in Figure 1E, the X-ray powder diffraction (XRD) pattern of BP showed several characteristic peaks located at 16.9°, 26.6°, 34.4°, 35.1°, 52.4°, 56.1°, and 56.9°, which were ascribed to the (020), (021),

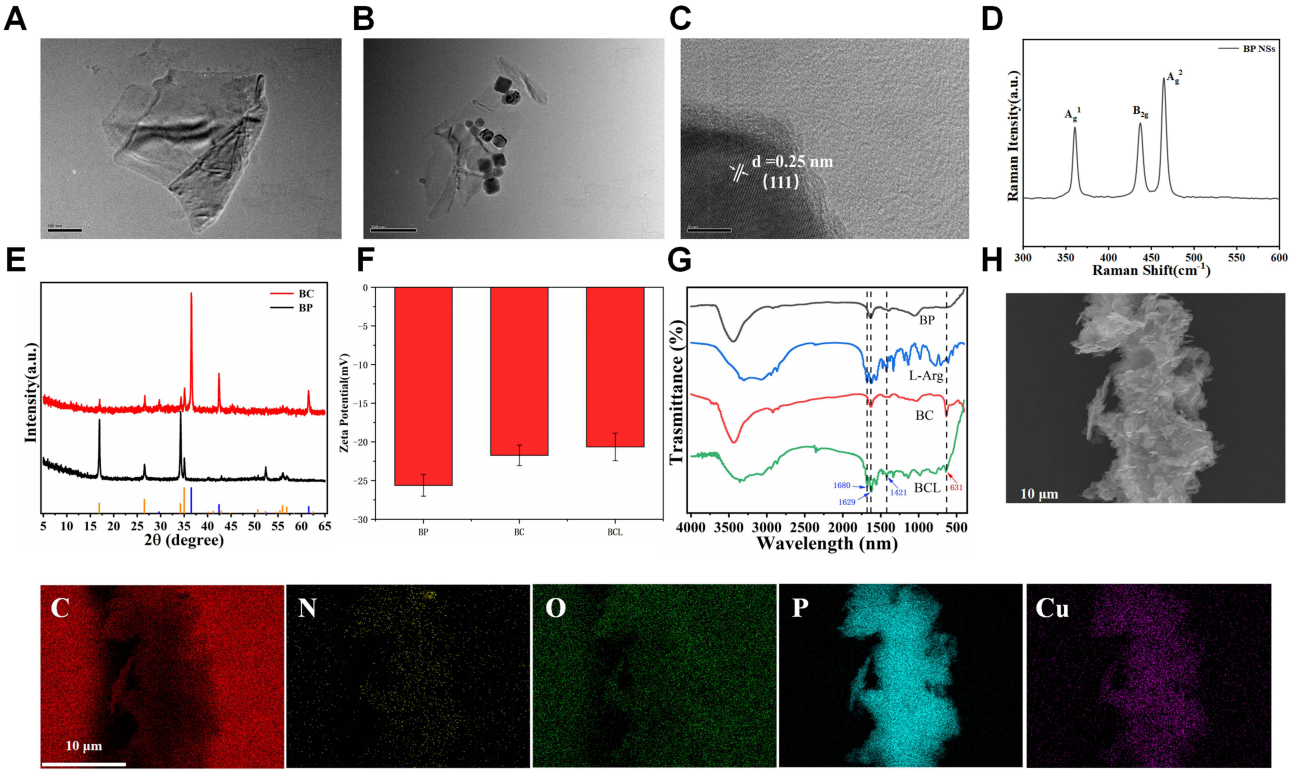

Figure 1 Characterization of nanoparticles (**A**) TEM image of BP NSs; (**B**) TEM and (**C**) HRTEM images of BCL; (**D**) Raman spectrum of BP NSs; (**E**) XRD patterns of BP NSs and BC; (**F**) Zeta potentials of BP, BC and BCL; (**G**) FT-IR spectrum of L-Arg, BP, BC and BCL; (**H**) SEM image and elemental mapping of BCL. C(red), N(yellow), O(green), P(blue) and Cu(purple).

(040), (060), (111), (151), and (061) lattice planes, respectively (JCPDS No. 73–1358).[39,40] The peaks at 29.8°, 36.6°, and 42.5° in the XRD spectrum of BC indicated the successful modification of Cu_2O on the BP nanosheets, which was consistent with the standard card of Cu_2O (JCPDS No. 77–0199).[4] Based on the above XRD results, BC was successfully obtained. L-Arg carried positive charge once they were dispersed into Tris·HCl solution (pH = 8.5). Thus, L-Arg can be loaded by negatively charged BC through electrostatic interaction. Figure 1F shows that the zeta potential of BP nanosheets was −25.6 mV, which further increased to −21.73 mV after in situ deposition of Cu_2O, and the potential after loading L-Arg was basically unchanged to −20.64 mV. The change in zeta potential further confirmed the successful loading of Cu_2O. The FT-IR spectra of the different nanomaterials are shown in Figure 1G. Compared to BP and BC, the very strong signal at 631 cm^{-1} was attributed to the stretching vibration of copper(I)–O (Cu_2O), which was consistent with previous literature.[41] After L-Arg loading, a new peak at 1680 cm^{-1} appeared in the FT-IR spectrum of BCL, which was attributed to–CO–NH–. The peak at 1421 cm^{-1} was assigned to −COO−, and the guanidine group of L-Arg at 1629 cm^{-1} could be distinguished.[42] FT-IR results confirmed the successful modification of Cu_2O and L-Arg. In addition, the element mapping image also showed a uniform distribution of C, N, O, P, and Cu elements, where the distribution of N elements proved the successful loading of L-Arg (Figure 1H).

In vitro Cu Ions Release, ROS and NO Production

BP has been shown to serve as a sonodynamic agent for the production of toxic ROS. Figure 2A shows the sonodynamic effects of BC using ABDA as the singlet oxygen ($^1O_2$) probe. With the prolongation of ultrasonic time, the relative

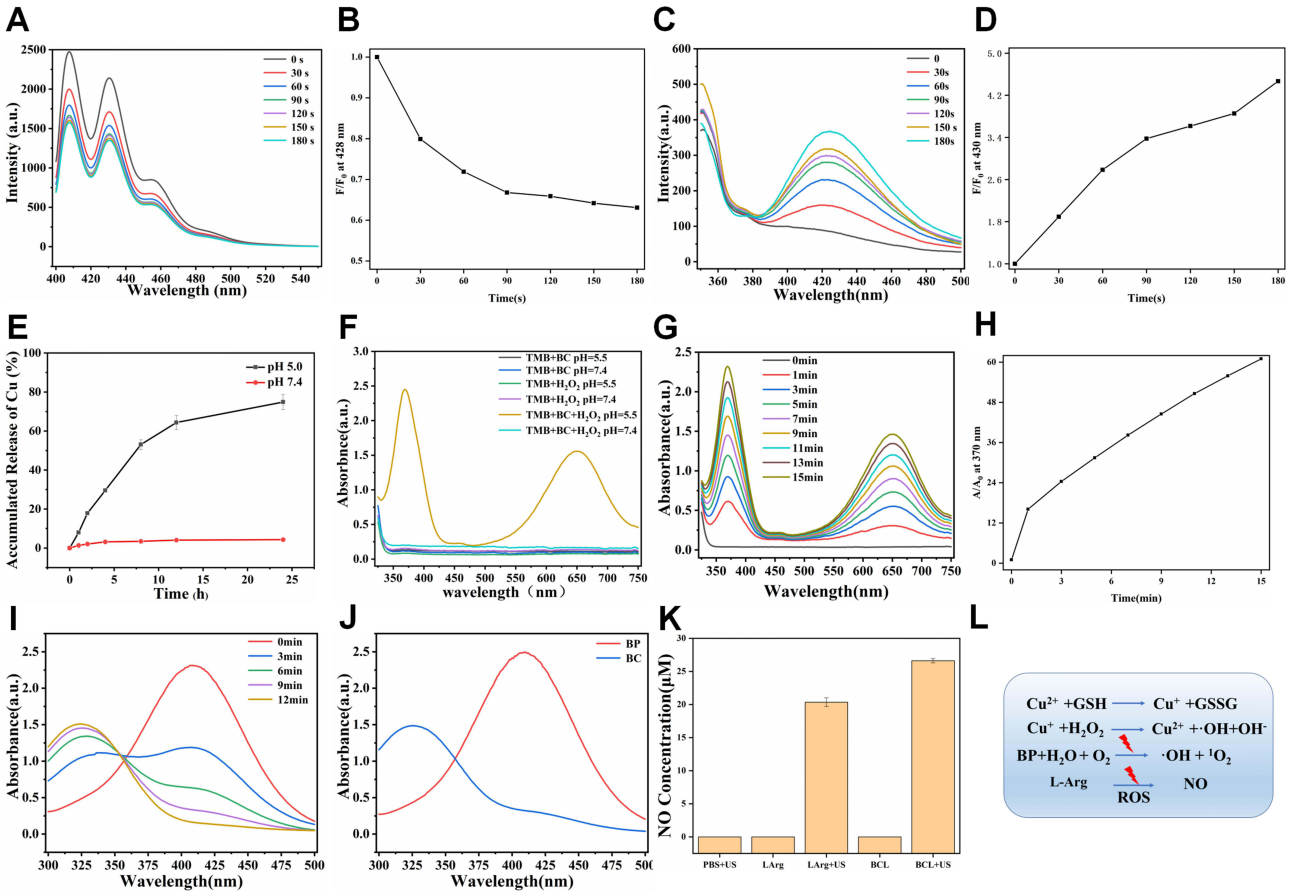

Figure 2 In vitro Cu release, ROS and NO production behaviors. (**A**) Time-dependent $^1O_2$ generation by BC detected by a ABDA probe under US irradiation; (**B**) Relative F/F_0 at 428 nm according to (**A**); (**C**) Time-dependent ·OH generation by BC using a PTA probe under US irradiation; (**D**) Relative F/F_0 at 430 nm according to (**C**); (**E**) The accumulated releases of Cu from BCL at pH 7.4 and 5.5; (**F**) UV–vis spectra of TMB incubated with single H_2O_2 or/and BC at pH 7.4 and 5.0; (**G**) UV–vis spectra of TMB incubated with H_2O_2 and BC with pH 5.0 at different time points; (**H**) Relative F/F_0 at 370 nm according to (**F**); (**I**) GSH consumption curve at different time points; (**J**) GSH consumption curve incubated with BP or BC; (**K**) NO concentration of different groups with/without US irradiation for 3 min; (**L**) The specific reaction processes. All the US irradiation treatments were proceeded under 1.0 MHz and 1.5 W/cm^2 and treatment was 3 min.

fluorescence peak intensity at 428 nm of ABDA decreased continuously from 1.0 to 0.63 (Figure 2B), indicating that BC continuously produced $^1O_2$ under ultrasonic stimulation. As shown in Figure 2C, the generation of ·OH was studied using PTA as a hydroxyl radical probe. The relative fluorescence peak intensity at 430 nm increased from 1.0 to 4.47 with the continuation of ultrasonic stimulation (Figure 2D), indicating that BC continuously produced ·OH under ultrasonic stimulation. These results indicated that BC can generate both $^1O_2$ and OH via ultrasonic stimulation.

Considering the weak acidity of the TME and lysosomes, the release behavior of Cu under different pH conditions was investigated. As shown in Figure 2E, the release rate was higher in the acidic environment than that in the alkaline environment. At 24 h, nearly 74.8% of Cu was released in an acidic environment (pH 5.5), whereas less than 5% of Cu was released in a weakly alkaline environment (pH 7.4). These results indicated that an acidic environment can effectively promote Cu release. Considering the high Fenton catalytic efficiency of Cu, the effect of Cu^{2+}/Cu^{+} on catalyzing H_2O_2 to generate ·OH was tested. The ox-TMB generated by the reaction of TMB with ·OH showed obvious absorption peaks at 370 and 650 nm (Figure 2F), indicating that the Fenton reaction can only be carried out in the presence of a catalyst, acidic environment, and hydrogen peroxide. As shown in Figure 2G, at pH 5.5, after adding H_2O_2, the specific absorption peak of TMB was significantly enhanced within 15 min. The quantitative relative absorption at 370 nm increased from 1.0 to 61.0 (Figure 2H), which proved that Cu^{2+}/Cu^{+} effectively catalyzed H_2O_2 to generate ·OH. Based on these results, we concluded that copper ions, H_2O_2 and acidic conditions were essential for the Fenton reaction. In addition, the amount of toxic OH depended on incubation time.

Intracellular GSH is an antioxidant that reduces ROS levels, thereby reducing the efficacy of ROS-based treatments. Cu^{2+} can effectively convert GSH to GSSG, while Cu^{2+} is reduced to Cu^{+}, thereby creating a cascade platform to reduce GSH content and enhance the ROS-based treatment effect. 5.5'-Dithiobis-2-nitrobenzoic acid (DTNB) reacts with GSH to generate 5-mercapto-2-nitrobenzoic acid with a maximum absorption signal at 412 nm. After Cu ions were released from Cu_2O, they were partially transformed into Cu^{2+}. As shown in Figure 2I, the signal at 412 nm weakened continuously over time, confirming the continuous consumption of GSH by Cu^{2+}. The results in Figure 2J show that Cu_2O, rather than BP, resulted in GSH depletion. As shown in Figure 2K, under the same L-Arg concentration and ultrasonic conditions, the concentration of NO produced by BCL was 23.1%, proving that L-Arg oxidation by ROS through ultrasonic stimulation was helpful for further NO generation. The specific reaction process is illustrated in Figure 2L.

Cytotoxic Effects and Underlying Mechanism Study

The anti-cancer effects of nanoparticles require effective cellular uptake; thus, we conducted confocal fluorescence imaging using 4T1 cells to show the cellular internalization of BP NSs. Rhodamine 6G dye was loaded into the BP NSs, and time-dependent cell distribution was monitored after co-culture for 1, 2, and 4 h. As shown in Figure S1, confocal images revealed that moderate BP NSs fluorescent signals were emitted from the tumor cell plasma at 1 h after incubation; remarkable accumulation of BP NSs reached the highest level at the second hour after incubation. However, the fluorescence intensity decreased sharply after an incubation time of 4 h. The quantitative analysis was shown in Figure S2. The cellular uptake of BP NSs indicated efficient drug delivery and possible good performance of anti-cancer ability. We further evaluated the in vitro toxicity of BCL on 4T1 cells. As displayed in Figure 3A, BCL exerted dose-dependent cytotoxicity in the presence or absence of US irradiation treatment. The addition of SDT exhibited enhanced anti-cancer efficacy in comparison with the non-irradiated groups, confirming a synergetic combined SDT therapy. Compared to the control group, cells treated with 40 μg/mL L-Arg showed no obvious inhibitory effects. The 4T1 cells were treated with the same amount of BC and BCL, which caused 23.35% and 64.89% cell death (Figure 3B). Moreover, additional US irradiation caused 39.77% and 79.68% toxicity in BC and BCL groups, respectively. These results indicated that BCL plus US caused severe cell death during tumor therapy.

As GSH is expressed at high levels in the tumor microenvironment to protect cancer cells from excessive ROS-based oxidative damages,[43–45] we used Cu_2O as an attractive Fenton-like catalyst to react with local GSH, thereby decreasing ROS consumption. Furthermore, BP has been utilized as a sonosensitizer to generate ROS under US stimulation, which is beneficial for NO generation in tumor cells.[46,47] To confirm this hypothesis, we investigated GSH depletion, intracellular ROS production, and nitric oxide (NO) release. As shown in Figure 3C, GSH decreased by 76% in the BC/BCL group

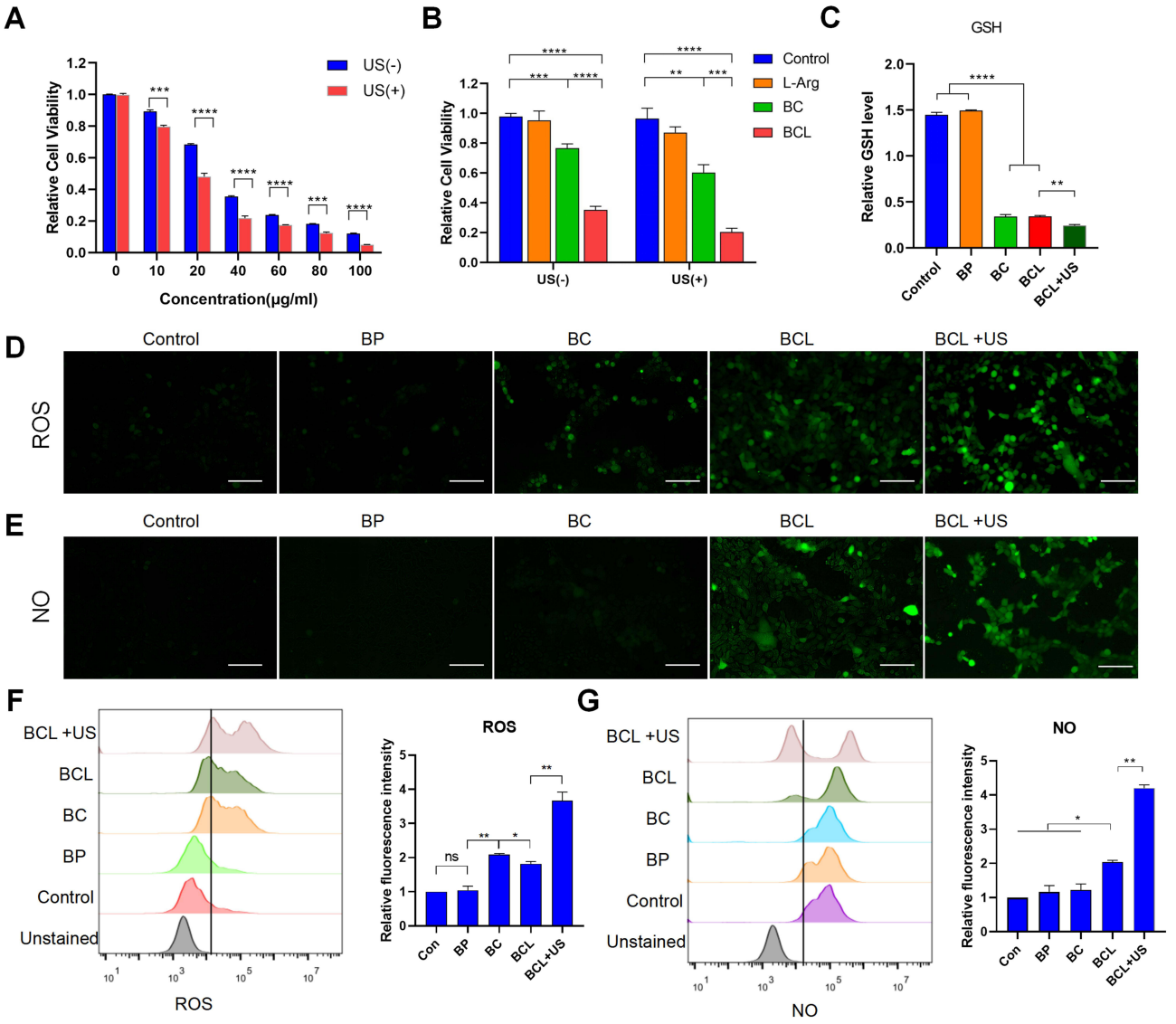

Figure 3 In vitro toxicity of BCL nanocomplex. (**A**) Cell viability of 4T1 cells treated with increasing dosage of BCL (0–100μg/mL), with or without US irradiation; (**B**) Cell viability of 4T1 cells treated with same amount of L-Arg, BC, BCL (40μg/mL) with or without US irradiation; (**C**) GSH content in cells treated with PBS, BP, BC, BCL, BCL +US; (**D**) Representative CLSM images of intracellular ROS in 4T1 cells in above groups; (**E**) Representative CLSM images of NO generation in 4T1 in above groups (Scale bars, 100 μm); FACS analysis of ROS (**F**) and NO (**G**) generation in 4T1 in above groups. *p< 0.05, **p < 0.01, ***p < 0.001. ****p < 0.0001.

compared with that in the control and BP groups. A 29% decrease in GSH content was observed in the BCL and US combination group, which confirmed the high GSH deletion capability of Cu ions via the Fenton reaction. As measured by 2.7 dichlorodihydro fluorescein diacetate (DCFH-DA), the capability of the nanoparticles to produce ROS was studied. As expected, no fluorescence was observed for the control group. Comparatively, BC-treated 4T1 cells showed brighter fluorescence than BP-treated cells, revealing the vital role of Cu_2^+ in GSH depletion and weakening of the ROS scavenging ability. The addition of US irradiation further induced ROS accumulation, which indicated the good performance of SDT (Figure 3D). Quantitative analysis of the images confirmed these results (Figure S3). Moreover, we verified the NO generation ability of various groups. The fluorescent NO probe of 3-amino-4-aminomethyl-2′,7′-difluorescein diacetate (DAF FM-DA) was used as an indicator. As shown in Figure 3E, negligible fluorescence signals were observed in the control, BP, and BC groups. In comparison, the cells treated with BCL showed higher levels of NO production. The strongest fluorescence was detected in cells treated with BCL and US irradiation, indicating that BCL+US produced large amounts of NO owing to the rapid oxidation of L-Arg by excessive ROS production. A quantitative analysis of the

fluorescence intensity is shown in Figure S4. FACS analysis further confirmed the above results (Figure 3F and G). Thus, we concluded that BCL exhibited outstanding cell-killing capacity through multiple mechanisms, including excessive ROS generation, GSH deletion, and massive NO production, suggesting their complementary roles in cell killing.

In vivo Synergistic Effect of BCL Therapy

To verify the therapeutic activity of BP-based nanocomposites against breast tumors, in vitro synergistic effects were evaluated using 4T1-bearing BALB/c mice as model tumors. The mice were randomly divided into six groups and locally injected with PBS, L-Arg, BC, or BCL at approximately the same tumor volume. Two additional groups (BC and BCL) were additionally treated with US irradiation after 6h of injection (1.0 MHz, 1.5W/cm^2, 5 min). This treatment was repeated on day 5 as shown in Figure 4A. The tumor volume of the mice was monitored every other day. Compared to the PBS group, the L-Arg group failed to suppress tumor growth, indicating that L-Arg alone had no tumor inhibition effect (Figure 4B). Mice injected with BC exhibited modest anti-tumor effects, with a 32% reduction in tumor weight compared to the control group. The group treated with BC and BCL group without US irradiation showed similar

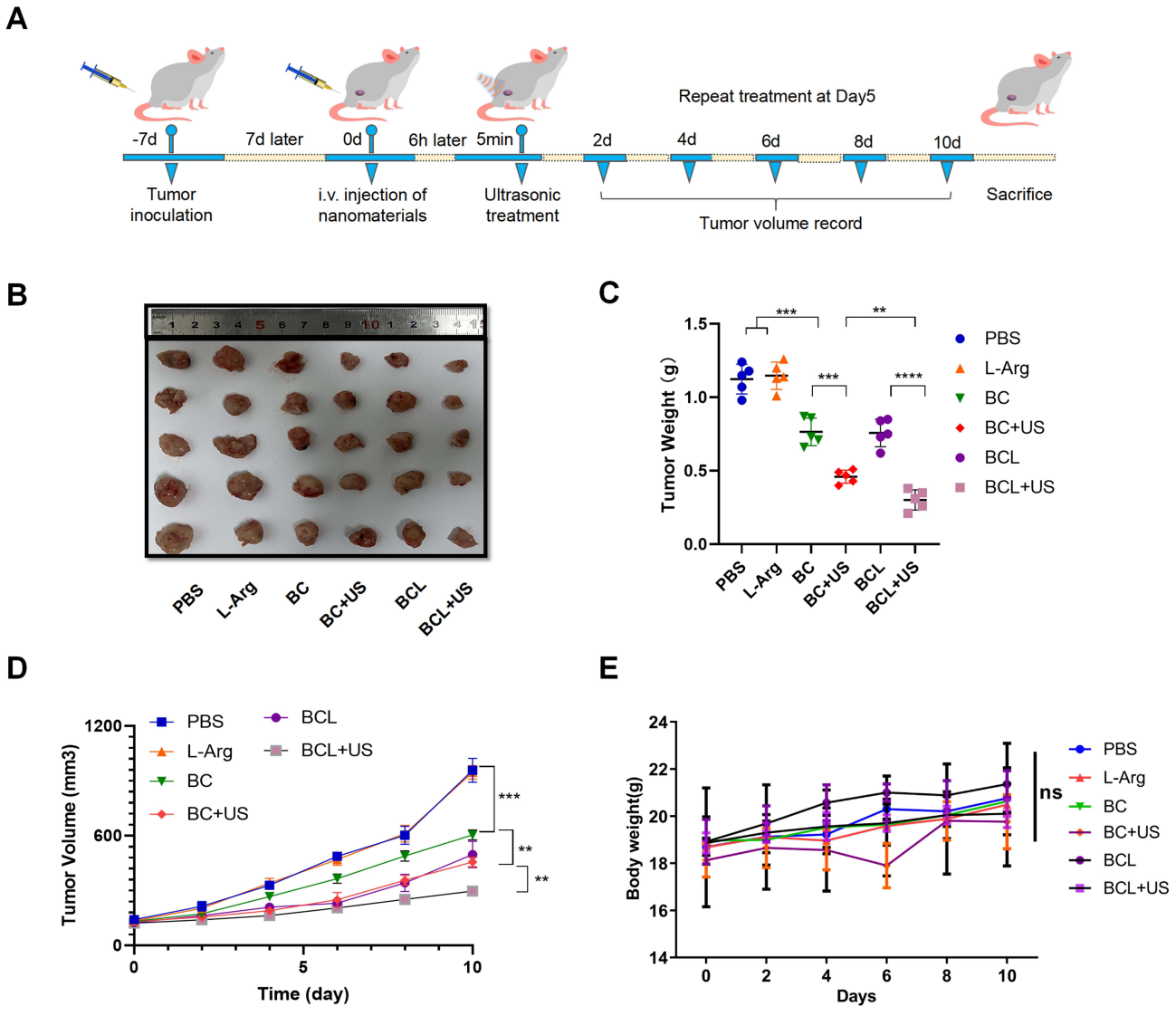

Figure 4 In vivo anti-tumor activity. (**A**) Time schedule of the treatment plan; (**B**) Representative tumor photographs of different mouse groups with locally injection of indicated treatments; (**C**) Tumor weight in above groups; (**D**)Tumor growth curves in above groups; (**E**) Body weight changes in above groups. Data are shown as mean ± SD (n = 3). **p < 0.01, ***p < 0.001. ****p < 0.0001.

therapeutic effects; the corresponding tumor weights were approximately 67.8% and 68.2% of those in the PBS group. The BCL+US group displayed the most potent tumor inhibition, with a 73.2% reduction in tumor weight (Figure 4C). Tumor volume confirmed the potent anti-cancer capacity of the combined therapy (Figure 4D). In addition, increased DHE fluorescence in BCL+US group indicated the abundance of ROS generation in BCL+US group (Figure S5). Furthermore, H&E staining was performed to examine pathological changes in the tumor sections. As expected, elevated nuclear damage and cellular edema were observed in the BCL + US group, indicating a potent anti-tumor efficacy (Figure S6). Additionally, no significant body weight loss or apparent histological abnormalities of the major organs (heart, liver, spleen, lungs, and kidneys) were observed, indicating the negligible organ toxicity and biocompatibility safety of BP-based nanoparticles (Figures 4E and S6).

The Enhanced Immune Response of BCL Therapy

Recent studies have focused on tumor-related antigens produced by severe apoptosis of cancer cells, which sequentially trigger anti-tumor immune responses.[45,46] Considering the complex regulatory effects of BP and NO on immune regulation, as well as ROS cascade-evoked immunogenic cell death, it is of great interest to investigate the influence of BCL on the immune response.[48,49] Next-generation RNA sequencing (NGS) was performed to evaluate the immune effects of BCL. The volcano plot showed the differentially expressed genes in 4T1 cells treated with PBS and BCL+US (Figure 5A). KEGG enrichment analysis revealed the activation of the immune system (Figure 5B). Gene set enrichment analysis (GSEA) further revealed that the majority of differentially expressed genes positively regulated the immune response (Figure 5C). Flow cytometry was used to analyze and quantify immune cells, including macrophages, myeloid-derived suppressor cells (MDSC), B lymphocytes, and T lymphocytes. Figure S7 illustrated the gating strategy in this study. As shown in Figure 6A and B, in the BCL+US treatment group, the proportion of CD45+/CD11b/+F4/80+

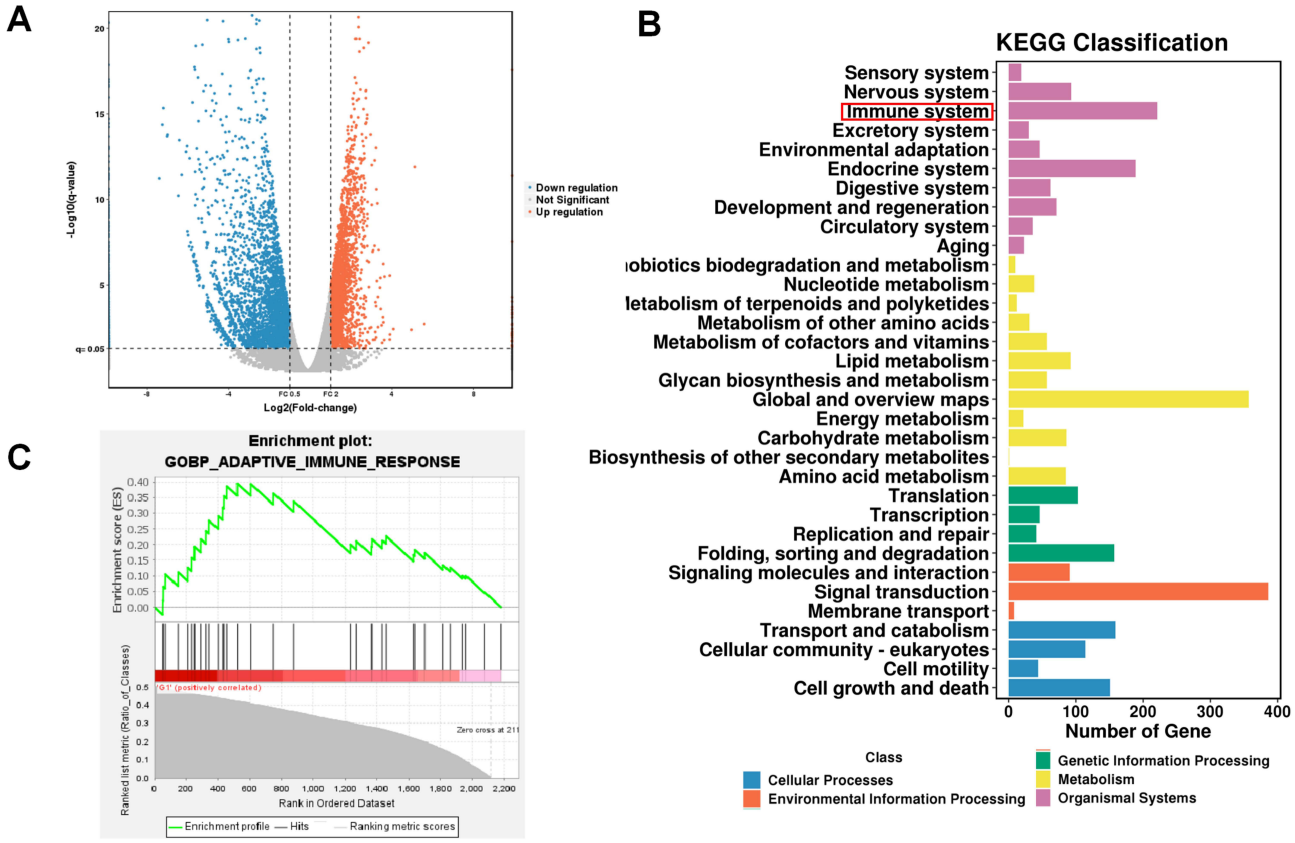

Figure 5 Bioinformatics analysis revealed the immune-regulation effects of BCL plus SDT therapy. (**A**) Volcano plots of the differentially expressed genes in 4T1 cells treated with PBS and BCL+US; (**B**) The top KEGG enrichment terms and (**C**) GSEA analyses of these genes enriched in (**A**).

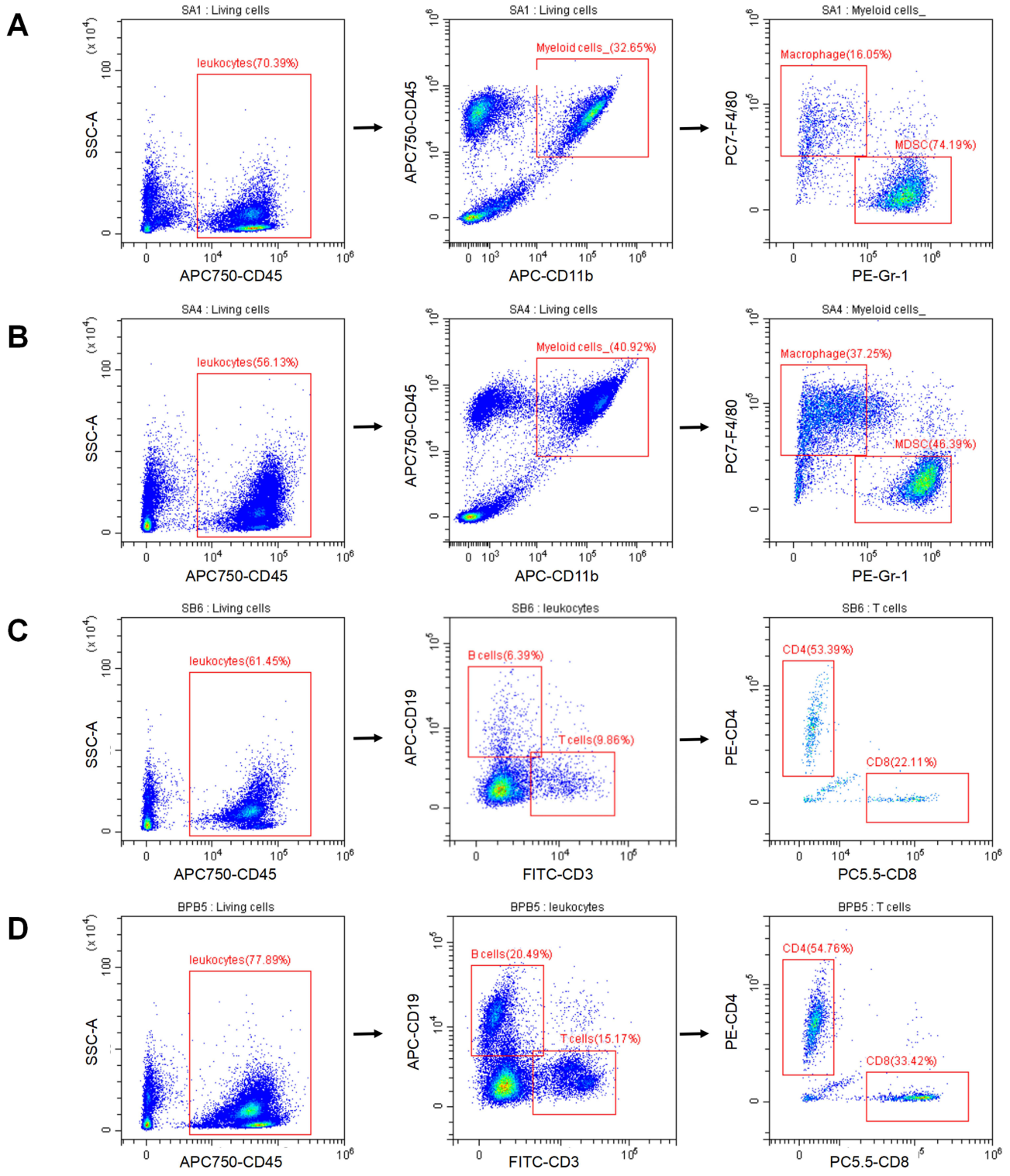

Figure 6 The in vivo immune responses. Populations of macrophages (CD45+/CD11b+/F4/80+) and MDSC (CD45+/CD11b+/Gr-1+) in (**A**) control group and (**B**) BCL+US group; Relative changes in B cells (CD45+/CD19+), CD4+T cells(CD45+/CD3+/CD4+) and CD8+T cells (CD45+/CD3+/CD8+) in (**C**) control group and (**D**) BCL+US group.

macrophages in tumor infiltration increased 2.36-fold compared to that in the control group (Figure S8). The representation of MDSC in the two groups showed that BCL+US reduced the percentage of immunosuppressive MDSC inside the tumor by 1.45-fold (Figure 6C and D). Subsequently, the number of CD8+-positive cells was approximately 1.68-fold higher than that in the control group. The proportion of CD4+ T-cells and B cells did not differ between the control and

BCL+US groups. To date, the potential effects and applications of BP-based particles on tumor immunological effects are still in the stage of continuous exploration. How particles interact with the immune response depends on their size, surface modification, protein corona formation, and cell types.[50] Previous studies have reported that BP-based nanoparticles interact with macrophages, which are immune cells responsible for engulfing and digesting foreign particles, pathogens, and cellular debris, ultimately modulating inflammation and immune activation.[51–53] In this case, multifunctional BCL promoted macrophage and CD8+ cell infiltration and inhibited immunosuppression infiltration of MDSC, demonstrating the prospect of modifying immunological anti-tumor responses.

Conclusions

In conclusion, a multi-functionalized BCL nanoplatform was fabricated for synergistic sonodynamic/chemical dynamic/nitric oxide gas therapy to enhance tumor-killing efficiency. Cu_2O consumed higher levels of GSH in tumor cells due to the Fenton reaction and the capability of BP to induce ROS generation under ultrasound irradiation, both of which can increase the efficacy of L-Arg for NO generation, consequently enhancing the anticancer effects by multiple mechanisms. In vitro investigations showed good anti-tumor effects of GSH deletion, ROS and NO production. In vivo studies demonstrated that BCL plus US treatment could significantly inhibit tumor growth and modify the immune anti-tumor response by promoting macrophage and CD8+ cell infiltration and inhibiting MDSC infiltration. This nanoplatform exhibited multifunctional characteristics for glutathione depletion-induced ROS/NO generation in cascade breast cancer therapy, paving the way for a new strategy for multitherapy.

Abbreviation

BP, Black Phosphorus; SDT, Sonodynamic therapy; CDT, Chemical dynamic therapy; PDT, Photodynamic therapy; LA, L-Arginine; NO, Nitric oxide; H&E, hematoxylin-eosin; DHE, dihydroethidium; Tregs, Regulatory T cells; GSH, Glutathione; CO, Carbon monoxide; KEGG, Kyoto Encyclopedia of Genes and Genomes; DEGs, differentially expressed genes; TCGA, The Cancer Genome Atlas; GSEA, Gene set enrichment analyses.

Disclosure

The authors have declared no conflicts of interest for this work.

References

1. Ding Y, Wan J, Zhang Z, Wang F, Guo J, Wang C. Localized Fe(II)-induced cytotoxic reactive oxygen species generating nanosystem for enhanced Anticancer Therapy. *ACS Appl Mater Interfaces*. 2018;10(5):4439–4449. doi:10.1021/acsami.7b16999
2. Zhou Z, Song J, Nie L, Chen X. Reactive oxygen species generating systems meeting challenges of photodynamic cancer therapy. *Chem Soc Rev*. 2016;45(23):6597–6626. doi:10.1039/c6cs00271d
3. Pan XT, Wang HY, Wang SH, et al. Sonodynamic therapy (SDT): a novel strategy for cancer nanotheranostics. *Sci China Life Sci*. 2018;61(4):415–426. doi:10.1007/s11427-017-9262-x
4. Wu HS, Chen FH, You CQ, Zhang Y, Sun BW, Zhu Q. Smart porous core-shell cuprous oxide nanocatalyst with high biocompatibility for acid-triggered Chemo/Chemodynamic Synergistic Therapy. *Small*. 2020;16(45). doi:10.1002/smll.202001805
5. Chen D, Zhong Z, Ma Q, Shao J, Huang W, Dong X. Aza-BODIPY-based nanomedicines in cancer phototheranostics. *ACS Appl Mater Interfaces*. 2020;12(24):26914–26925. doi:10.1021/acsami.0c05021
6. Shao JD, Xie HH, Huang H, et al. Biodegradable black phosphorus-based nanospheres for in vivo photothermal cancer therapy. *Nat Commun*. 2016;7. doi:10.1038/ncomms12967
7. Shao JD, Ruan CS, Xie HH, et al. Black-phosphorus-incorporated hydrogel as a sprayable and biodegradable photothermal platform for postsurgical treatment of cancer. *Adv Sci*. 2018;5(5). doi:10.1002/advs.201700848
8. Anju S, Ashtami J, Mohanan PV. Black phosphorus, a prospective graphene substitute for biomedical applications. *Mater Sci Eng C Mater Biol Appl*. 2019;97:978–993. doi:10.1016/j.msec.2018.12.146
9. Chen W, Ouyang J, Liu H, et al. Black phosphorus nanosheet-based drug delivery system for synergistic Photodynamic/Photothermal/Chemotherapy of Cancer. *Adv Mater*. 2017;29(5).1603864
10. Qian X, Zheng Y, Chen Y. Micro/Nanoparticle-Augmented Sonodynamic Therapy (SDT): breaking the Depth Shallow of Photoactivation. *Adv Mater*. 2016;28(37):8097–8129. doi:10.1002/adma.201602012
11. Yang Y, Wang X, Qian H, Cheng L. Titanium-based sonosensitizers for sonodynamic cancer therapy. *Appl Mater Today*. 2021;25:101215. doi:10.1016/j.apmt.2021.101215
12. Ning S, Dai X, Tang W, et al. Cancer cell membrane-coated C-TiO2 hollow nanoshells for combined sonodynamic and hypoxia-activated chemotherapy. *Acta Biomater*. 2022;152:562–574. doi:10.1016/j.actbio.2022.08.067

13. Wang H, Yang X, Shao W, et al. Ultrathin black phosphorus nanosheets for efficient singlet oxygen generation. *J Am Chem Soc*. 2015;137(35):11376–11382. doi:10.1021/jacs.5b06025
14. Yang X, Wang D, Shi Y, et al. Black phosphorus nanosheets immobilizing ce6 for imaging-guided photothermal/photodynamic cancer therapy. *ACS Appl Mater Interfaces*. 2018;10(15):12431–12440. doi:10.1021/acsami.8b00276
15. Liu Y, Li Z, Fan F, et al. Boosting antitumor sonodynamic therapy efficacy of black phosphorus via covalent functionalization. *Adv Sci*. 2021;8(20):e2102422. doi:10.1002/advs.202102422
16. Dong W, Wang H, Liu H, et al. Potential of black phosphorus in immune-based therapeutic strategies. *Bioinorg Chem Appl*. 2022;2022:3790097. doi:10.1155/2022/3790097
17. Liu CH, Wang DD, Zhang SY, et al. Biodegradable biomimic copper/manganese silicate nanospheres for chemodynamic/photodynamic synergistic therapy with simultaneous glutathione depletion and hypoxia relief. *Acs Nano*. 2019;13(4):4267–4277. doi:10.1021/acsnano.8b09387
18. Ma BJ, Wang S, Liu F, et al. Self-assembled copper amino acid nanoparticles for in situ glutathione and h2o2 sequentially triggered chemodynamic therapy. *J Am Chem Soc*. 2019;141(2):849–857. doi:10.1021/jacs.8b08714
19. Dai YL, Yang Z, Cheng SY, et al. Toxic reactive oxygen species enhanced synergistic combination therapy by self-assembled metal-phenolic network nanoparticles. *Adv Mater*. 2018;30(8). doi:10.1002/adma.201704877
20. Lin LS, Song JB, Song L, et al. Simultaneous Fenton-like ion delivery and glutathione depletion by mno2-based nanoagent to enhance chemodynamic therapy. *Angew Chem Int Edit*. 2018;57(18):4902–4906. doi:10.1002/anie.201712027
21. Huang P, Qian XQ, Chen Y, et al. metalloporphyrin-encapsulated biodegradable nanosystems for highly efficient magnetic resonance imaging-guided sonodynamic cancer therapy. *J Am Chem Soc*. 2017;139(3):1275–1284. doi:10.1021/jacs.6b11846
22. Zhang C, Chen WH, Liu LH, Qiu WX, Yu WY, Zhang XZ. An O-2 Self-supplementing and reactive-oxygen-species-circulating amplified nanoplatform via H2O/H2O2 splitting for tumor imaging and photodynamic therapy. *Adv Funct Mater*. 2017;27(43). doi:10.1002/adfm.201700626
23. Gong NQ, Ma XW, Ye XX, et al. Carbon-dot-supported atomically dispersed gold as a mitochondrial oxidative stress amplifier for cancer treatment. *Nat Nanotechnol*. 2019;14(4):379-+. doi:10.1038/s41565-019-0373-6
24. Yin SY, Song GS, Yang Y, et al. Persistent regulation of tumor microenvironment via circulating catalysis of MnFe2O4@Metal-organic frameworks for enhanced photodynamic therapy. *Adv Funct Mater*. 2019;29(25). doi:10.1002/adfm.201901417
25. Sang YJ, Cao FF, Li W, et al. Bioinspired construction of a nanozyme-based H2O2 homeostasis disruptor for intensive chemodynamic therapy. *J Am Chem Soc*. 2020;142(11):5177–5183. doi:10.1021/jacs.9b12873
26. Tang ZM, Liu YY, He MY, Bu WB. Chemodynamic therapy: tumour microenvironment-mediated Fenton and Fenton-like reactions. *Angew Chem Int Edit*. 2019;58(4):946–956. doi:10.1002/anie.201805664
27. Ren ZG, Sun SC, Sun RR, et al. A metal-polyphenol-coordinated nanomedicine for synergistic cascade cancer chemotherapy and chemodynamic therapy. *Adv Mater*. 2020;32(6). doi:10.1002/adma.201906024
28. Soltani T, Lee BK. Enhanced formation of sulfate radicals by metal-doped BiFeO3 under visible light for improving photo-Fenton catalytic degradation of 2-chlorophenol. *Chem Eng J*. 2017;313:1258–1268. doi:10.1016/j.cej.2016.11.016
29. Poyton MF, Sendecki AM, Cong X, Cremer PS. Cu2+ binds to phosphatidylethanolamine and increases oxidation in lipid membranes. *J Am Chem Soc*. 2016;138(5):1584–1590. doi:10.1021/jacs.5b11561
30. Bokare AD, Choi W. Review of iron-free Fenton-like systems for activating H2O2 in advanced oxidation processes. *J Hazard Mater*. 2014;275:121–135. doi:10.1016/j.jhazmat.2014.04.054
31. Wang L, Chang Y, Feng YL, et al. Nitric oxide stimulated programmable drug release of nanosystem for multidrug resistance cancer therapy. *Nano Lett*. 2019;19(10):6800–6811. doi:10.1021/acs.nanolett.9b01869
32. Zhou Y, Yu WQ, Cao J, Gao HL. Harnessing carbon monoxide-releasing platforms for cancer therapy. *Biomaterials*. 2020;255:120193. doi:10.1016/j.biomaterials.2020.120193
33. Yang ZB, Luo Y, Hu YA, et al. Photothermo-promoted nanocatalysis combined with H2S-mediated respiration inhibition for efficient cancer therapy. *Adv Funct Mater*. 2021;31(8).2007991
34. Wang MF, Hou ZY, Liu SN, et al. A multifunctional nanovaccine based on l-arginine-loaded black mesoporous titania: ultrasound-triggered synergistic cancer sonodynamic therapy/gas therapy/immunotherapy with remarkably enhanced efficacy. *Small*. 2021;17(6).2005728
35. Irvine DJ, Dane EL. Enhancing cancer immunotherapy with nanomedicine. *Nat Rev Immunol*. 2020;20(5):321–334. doi:10.1038/s41577-019-0269-6
36. Yu M, Duan X, Cai Y, et al. Multifunctional nanoregulator reshapes immune microenvironment and enhances immune memory for tumor immunotherapy. *Adv Sci*. 2019;6(16):1900037. doi:10.1002/advs.201900037
37. Wang J, Chen W, Du W, et al. ROS generative black phosphorus-tamoxifen nanosheets for targeted endocrine-sonodynamic synergistic breast cancer therapy. *Int j Nanomed*. 2023;18:2389–2409. doi:10.2147/IJN.S406627
38. Wang YX, Huang D, Zhu XZ, et al. Surfactant-free synthesis of Cu2O hollow spheres and their wavelength-dependent visible photocatalytic activities using LED lamps as cold light sources. *Nanoscale Res Lett*. 2014;9. doi:10.1186/1556-276X-9-624
39. Cai W, Cai TM, He LX, et al. Natural antioxidant functionalization for fabricating ambient-stable black phosphorus nanosheets toward enhancing flame retardancy and toxic gases suppression of polyurethane. *J Hazard Mater*. 2020;387:121971. doi:10.1016/j.jhazmat.2019.121971
40. Tao W, Zhu XB, Yu XH, et al. Black phosphorus nanosheets as a robust delivery platform for cancer theranostics. *Adv Mater*. 2017;29(1). doi:10.1002/adma.201603276
41. Chen C, Xu HY, Xu L, Zhang FJ, Dong JK, Wang H. One-pot synthesis of homogeneous core-shell Cu2O films with nanoparticle-composed multishells and their photocatalytic properties. *RSC Adv*. 2013;3(47):25010–25018. doi:10.1039/c3ra43450h
42. He S, Gao YY, Zhao ZY, et al. Fully bio-based phytic acid-basic amino acid salt for flame-retardant polypropylene. *ACS Appl Polymer Mater*. 2021;3(3):1488–1498. doi:10.1021/acsapm.0c01356
43. Cook JA, Gius D, Wink A, Krishna MC, Russo A, Mitchell JB. Oxidative stress, redox, and the tumor microenvironment. *Semin Radiat Oncol*. 2004;14(3):259–266. doi:10.1016/j.semradonc.2004.04.001
44. Cairns RA, Harris IS, Mak TW. Regulation of cancer cell metabolism. *Nat Rev Cancer*. 2011;11(2):85–95. doi:10.1038/nrc2981
45. Catalano V, Turdo A, Di Franco S, Dieli F, Todaro M, Stassi G. Tumor and its microenvironment: a synergistic interplay. *Semin Cancer Biol*. 2013;23(6 Pt B):522–532. doi:10.1016/j.semcancer.2013.08.007
46. Szatrowski TP, Nathan CF. Production of large amounts of hydrogen peroxide by human tumor cells. *Cancer Res*. 1991;51(3):794–798.

47. Mates JM, Sanchez-Jimenez FM. Role of reactive oxygen species in apoptosis: implications for cancer therapy. *Int J Biochem Cell Biol*. 2000;32(2):157–170. doi:10.1016/S1357-2725(99)00088-6
48. Sung Y-C, Jin P-R, Chu L-A, et al. Delivery of nitric oxide with a nanocarrier promotes tumour vessel normalization and potentiates anti-cancer therapies. *Nat Nanotechnol*. 2019;14(12):1160–1169. doi:10.1038/s41565-019-0570-3
49. Kim J, Sestito LF, Im S, Kim WJ. Thomas, Poly(cyclodextrin)-polydrug nanocomplexes as synthetic oncolytic virus for locoregional melanoma chemoimmunotherapy. *Adv Funct Mater*. 2020;30(16).1908788
50. Cheng M, Shi H, Xu T, Jiang W, Tang BZ, Duo Y. High-dimensional single-cell cartography tracking of immune cells subpopulation of mice peripheral blood treated with gold nanorods and black phosphorus nanosheets. *Nano Today*. 2022;47:101666. doi:10.1016/j.nantod.2022.101666
51. Zhang X, Tang J, Li C, Lu Y, Cheng L, Liu J. A targeting black phosphorus nanoparticle based immune cells nano-regulator for photodynamic/photothermal and photo-immunotherapy. *Bioact Mater*. 2021;6(2):472–489. doi:10.1016/j.bioactmat.2020.08.024
52. Mo J, Xie Q, Wei W, Zhao J. Revealing the immune perturbation of black phosphorus nanomaterials to macrophages by understanding the protein Corona. *Nat Commun*. 2018;9(1). doi:10.1038/s41467-018-04873-7
53. Qin H, Chen J, Li Y, et al. Inflammatory response induced by black phosphorus nanosheets in mice and macrophages. *Sci Total Environ*. 2021;782:146860. doi:10.1016/j.scitotenv.2021.146860